A Multi-scale Geometrical Model for Finite Element Analyses of Three-dimensional Angle-Interlock Woven Composite under Ballistic Penetration

Kun Luan[1]**, Baozhong Sun**[1] **and Bohong Gu**[1,2]

Abstract: This paper reports finite element multi-scale simulations of ballistic impact damage of three-dimensional angle-interlock woven composite (3DAWC) penetrated under a hemispherical rigid projectile. A multi-scale geometrical model of the 3DAWC was established for the numerical simulation. The multi-scale geometrical model of the 3DAWC consists two parts: one is the microstructure model and another is the continuum model. The microstructure model has the same microstructure with that of the 3DAWC composite panel, including the fiber tows' diameter, fiber tow configuration and fiber volume fraction. The continuum model has the same mechanical properties with the 3DAWC. The commercial-available finite element software package Ls-Dyna was used for the ballistic penetration damage simulations. The ballistic impact damages of the 3DAWC and the residual velocities of the rigid projectile under the different strike velocities have been calculated and compared with those in experimental. Good agreements were found between the finite element analyses (FEA) and experimental. From the FEA results, the impact damage development and the stress wave propagation in the 3DAWC panel can be extracted to find the influence of the microstructure parameters of the 3DAWC on the ballistic impact capacity. With the efforts, the ballistic impact capacity of the 3DAWC could be designed in a more precise way.

Keywords: 3-D angle-interlock woven composite (3DAWC); multi-scale geometrical model; microstructure; ballistic impact; finite element analysis (FEA)

1   Introduction

Three-dimensional angle-interlock woven composite (3DAWC) has higher inter-laminar shear strength and fracture toughness than the laminated composite be-

---

[1] College of Textiles, Key Laboratory of high-performance fibers & products, Donghua University, Shanghai, China, 201620

[2] Corresponding author, E-mail: gubh@dhu.edu.cn, Tel: +86-21-67792661 Fax: +86-21-67792627

cause of the integrated woven structure. Especially, the angle-interlock yarns in the woven structure leads the higher delamination resistance. The 3DAWC will have higher impact damage tolerance than that of laminates. Compared with 3-D orthogonal woven fabric, the 3-D angle-interlock woven fabric can be woven with traditional looms in a high efficiency. The manufacturing cost of the 3-D angle-interlock woven fabric is lower than the 3-D orthogonal woven fabric. Therefore the 3DAWCs have high impact damage tolerance and low manufacturing cost. All these advantages will lead the great potential of the applications of the 3DAWC to aircraft, high speed vehicle and protective materials.

The impact behaviors of the 3DAWC have been reported in several references. Very early, Ko [Ko and David (1986)] compared the drop weight impact behaviors of 2-D biaxial woven and 3-D XYZ orthogonally woven composites. Kuo [Kuo and Lee (1998)] examined the impact response of three-dimensionally woven fabric composites using consolidated rods in the axial direction. Chiu [Chiu, Lai and Wu (2004)] conducted instrumented drop weight impact and compression-after-impact tests (CAI) and found the 3-D interlock woven composites exhibited a smaller impact damage area and higher % residual strength than the 2-D woven laminated composites. Gama [Gama, Bogdanovich, Coffelt, Haque, Rahman and Gillespie (2005)] performed numerical simulation of ballistic impact, damage and penetration of a single layer 3-D orthogonal weave fabric composite. A unit cell model (UCM) of the composite was developed using fabric design and processing parameters, as well as control measurements taken on the preform and the composite laminate. Tabiei [Tabiei and Ivanov (2007)] created a simple 3-D micromechanical model for woven fabric composites for impact simulations using transient finite element codes. More recently, Kim [Kim, Ji, and Paik (2008)] examined the possibilities of the virtual tests of composite structures by simulating mechanical behaviors by using supercomputing technologies for cross-ply laminates and 3-D orthogonal woven composites. Chen [Chen and Yang (2010a); Chen and Yang (2010b)] reported the ballistic performance of angle-interlock fabrics and found that the angle-interlock fabric is not less than the conventional fabric constructions used for body armor against ballistic impact. They also presented the mathematical modeling of molding of angle-interlock fabrics to form the front panel of female body armor. Boussu [Boussu (2011)] comprehensively reviewed the different types of the warp interlock to be defined according to their performance on delamination and impact resistances. Cuong [Cuong, Boussu, Kanit, Crepin, and Imad (2011)] presented a finite element model to describe a ballistic impact on a 3D warp interlock Kevlar KM2 fabric and studied the effect of friction onto the ballistic impact behavior of this textile interlock structure. The authors of this paper reported a series of investigations on the impact behaviors of 3-D angle-interlock woven fabrics

and composites, including the ballistic impact behaviors, high strain rate behaviors [Sun and Gu (2007); Li, Sun and Gu (2010); Cui, Sun and Gu, (2011); Jin, Sun and Gu (2011)]. However, the ballistic impact damage of the 3DAWC has not been investigated at the microstructure level. The investigation of the impact damage at microstructure level can uncover the damage mechanism that is often invisible in continuum level.

The 3DAWCs have the great potential applications to ballistic protection for its merits of near-net-shape and excellent delamination and damage tolerance. This paper will report the finite element simulations of ballistic penetration damage of the 3DAWC based on a multi-scale geometrical model. The impact damage morphologies will be presented at the microstructure level. Furthermore, the energy absorptions and the stress wave propagation in the 3DAWC panel will be given at the multi-scale model for illustrating the ballistic penetration damage mechanisms.

2 Target-projectile system

2.1 Target panel

The 3-D angle-interlock woven fabric (3DAWF) has been widely used in textile composites manufacturing due to its higher weaving efficiency and delamination resistance. Compared with 3-D woven structure formed by stitched fabric, there is no damage in warp and weft yarns caused by stitching. The woven architecture of the 3DAWF can be easily adjusted to manufacture the composite panels with different thicknesses. By increasing warp yarn layers, high thickness fabric can be woven. In general, the warp yarns in the 3DAWF structure are crimp while the weft yarns are straight.

The 3DAWF reported in this paper was woven by interlacing two adjacent layers of weft yarns with warp yarns. Such a structure will enable the fabric more flexible. The warp yarns and weft yarns are both the Twaron filament tows manufactured by Akzo Nobel. Twaron® is a kind of aramid fiber (poly paraphenylene terephtalamide, PPTA) similar to that of Kevlar® of Dupont De Nemours. The fineness of the warp and weft filament tows is 3360 dtex and 6720 dtex respectively (tex is a basic textile unit of linear density — the weight in grams of a fiber in a length of one kilometer. Units = g/km = (g/cm) $\times$ 10-5, 10 dtex=1tex). The specifications of the 3DAWF are listed in Table 1.

Unsaturated polyester resin was injected into the preform adopting VARTM (vacuum assisted resin transfer molding) technique to form the 3DAWC. The fiber volume fraction of the 3DAWC is about 44.6%. The cross-section of the 3DAWC is shown in Fig. 1, where the configuration of interlock yarns in the thickness direction can be observed. After consolidation of the unsaturated polyester resin, the

Table 1: Specifications of the 3-D angle interlock woven fabric

Fabric type	Count (dtex) warp/weft	Material type warp/weft	Densities (ends and picks/1cm)	Fabric weight (g/m^2)
Angle-interlock	1680×2/ 1680×4	1680 dtex Kevlar/ Kevlar	8×11/4×12	8600

Table 2: Specifications of the 3-D angle interlock woven composite panel

Length (mm)	Width (mm)	Thickness (mm)	Area density (g/m^2)	Panel weight (g)
192	214	10.8	12800	524.75

Table 3: Parameters of Twaron® untwisted filament tows

Mass density ρ(g/cm^3)	Longitudinal tensile modulus E_{f1}(GPa)	Transverse tensile modulus E_{f2}(GPa)	Shear modulus G_f(GPa)	Poisson's ratio γ_f
1.44	116	50	18.2	0.2

Table 4: Parameters of unsaturated polyester resin

Tensile modulus E_m(GPa)	Shear modulus G_m(GPa)	Poisson's ratio γ_f	Tensile strength X_T(MPa)	Compressive strength X_C(MPa)	Shear strength S_S(MPa)
6.8	2.46	0.38	388.4	366.8	153.6

composite sample was cut according to the in-plane dimension of 192mm×214mm. The thickness of the composite panel is 10.8mm. Table 2 lists the parameters of the 3DAWC panel for the ballistic impact tests. Table 3 and Table 4 are the mechanical parameters of the fiber tows and the resin respectively.

2.2 Projectile

As shown in Fig. 2(a), a hemispherical cylindrical steel projectile of diameter 7.62mm was applied in the ballistic impact test. Fig.2 (b) is the geometrical model of the projectile in finite element simulation. The projectile, whose mass density
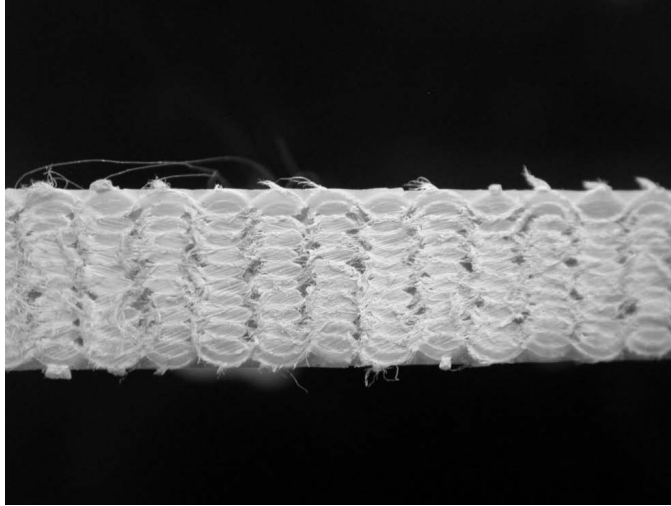
Figure 1: Cross-section photograph of the 3-D angle-interlock woven composite

is 7.8 g/cm^3, is 5.59 g in weight. This projectile is named as 'Type 56' according to the Chinese military standard. As an isotropic material, the Young's modulus of the projectile is 200GPa and the Poisson's ratio is 0.2. The projectile was propelled along a ballistic barrel by using gunpowder and the strike velocity of the projectile could be controlled by adjusting the weight of gunpowder. Two laser-diode pairs were used to measure the strike velocities and residual velocities of the projectile before and after ballistic penetration.

2.3 *Ballistic impact tests*

A series of ballistic impact tests were conducted with Type 56 projectiles to determine the strike and residual velocities of the projectiles. The tests were conducted at No.53 Institute of China Ammunition Co. Ltd. The four sides of the composite target were fixed and the impact point was at the center of the composite panel. The minimum strike velocity was designed as 210m/s to capture the projectile, and the maximum strike velocity was 550m/s to perforate the composite, respectively.

3 Multi-scale geometrical model of the 3DAWC

The multi-scale geometrical model for the woven fabric and composites in impact damage simulation is very popular way to calculate the impact damage at the yarn level with the appropriate computing time. Such kind of models and techniques can be found in references [Nilakantan, Keefe, Bogetti and Gillespie, (2010); Nilakan-
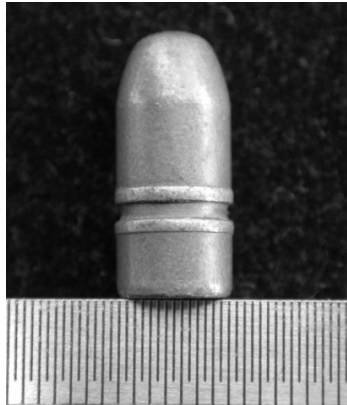
(a)   Photograph of the hemispherical cylindrical steel projectile
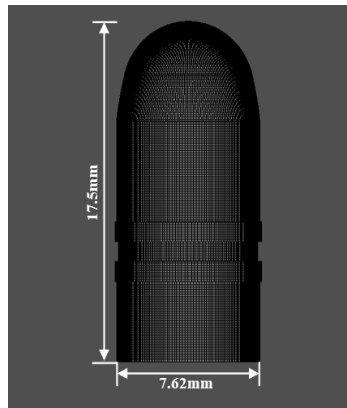

(b) Finite element geometrical model

Figure 2: Photograph of the hemispherical cylindrical steel projectile and finite element geometrical model

tan, Keefe, Bogetti, Adkinson and Gillespie (2010); Tserpes, Labeas and Pantelakis (2010); Barauskas and Abraitiene (2007); Nadler, Papadopoulos and Steigmann (2006); Zohdi and Powell (2006); Zhang, Y. X. and Zhang, H. S. (2010)]. This kind of model allows the capturing of complex projectile-fabric and yarn-yarn level interactions in acceptable computational resources. This technique involves modeling the fabric using a yarn level architecture around the impact region and a homogenized or membrane type architecture at far field regions.

As for the 3DAWC in this paper, a multi-scale geometrical model is also estab-
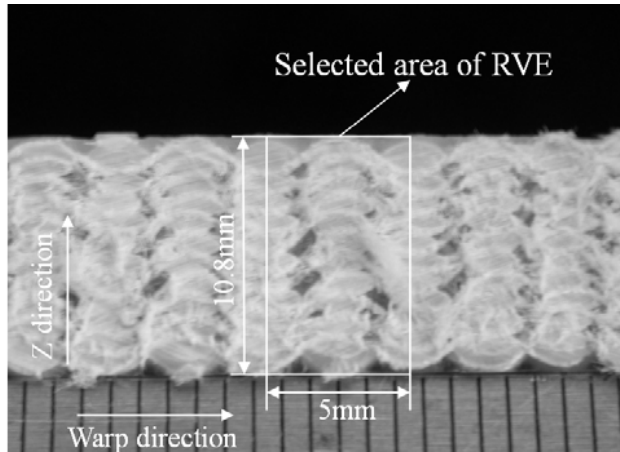
(a)
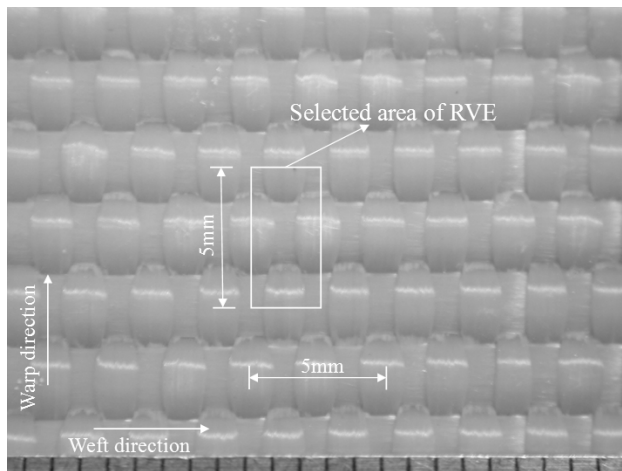
(b)

Figure 3: Geometrical parameters of the 3-D angle-interlock woven composite

lished. The multi-scale geometrical model of the 3DAWC consists two parts: one is the microstructure model around the impact position and another is the continuum model in the rest parts of composite panel.

3.1   Microstructure model

Assuming the cross-section of the fiber tow is a circle.

Fig.3 shows the geometrical parameters of the 3DAWC, where the size of the thickness and woven fabric construction are shown.

Based on the definition of the 'dtex' as described in Section 2.1 and the data in Table 1,

$$\text{dtex} = \frac{G}{L \times 10000}$$

$$G_{warp} = 2G_{weft}$$

Considering the same density of warp yarns and weft yarns and the idealized cross sectional area of yarn, then the relationships of the diameters between weft yarns and warp yarns is:

$$d_{weft} = \sqrt{2}d_{warp} \tag{1}$$

where G is the yarn mass (g) and L is the yarn length (m), d_{warp} and d_{weft} are the diameters of warp and weft yarns respectively.

The thickness of the 3DAWC panel T can be expressed as:

$$T = N_{warp}d_{warp} + N_{weft}d_{weft} \tag{2}$$

where N_{warp} and N_{weft} are the number of warp and weft respectively.

From the equations (1) and (2), the diameter of the warp yarn and weft yarn can be calculated.

Fig.4 shows 3-D angle-interlock structure and axis line of warp yarn. In the 3-D angle-interlock woven fabric, the weft yarns were bonded by the warp yarns layer-to-layer. From the diameter of the warp and weft yarns, and the fabric construction as shown in Fig.4 (a), the microstructure model of the 3DAWC could be obtained and shown in Fig.5. In Fig.5, the microstructure model consists of the warp yarns, weft yarns and resins. All the geometrical parameters in Fig.5 were derived from the same microstructure and fiber volume fraction with those of 3DAWC in experimental.
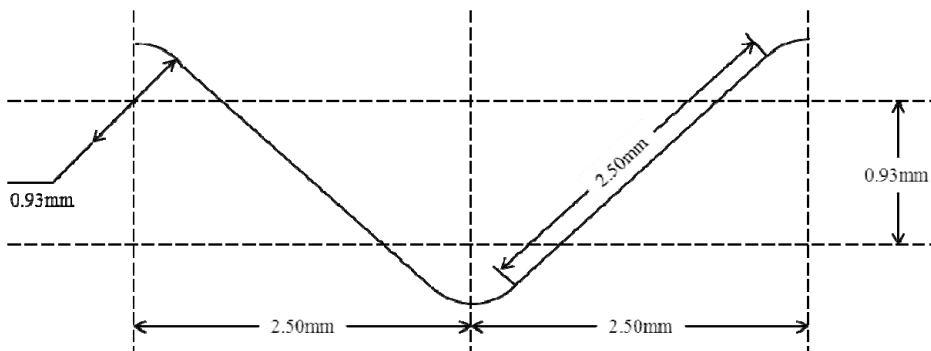
3.2   Continuum model

The microstructure model is based on the observations of the 3DAWC microstructure. For a representative volume element (RVE) of the microstructure model, Fig.5 shows the mesh scheme by the four-node tetrahedron element. There are 78475 elements for this RVE. This huge number of elements requires large capacity of computer. If the whole composite panel is meshed, it would have more than billions elements.
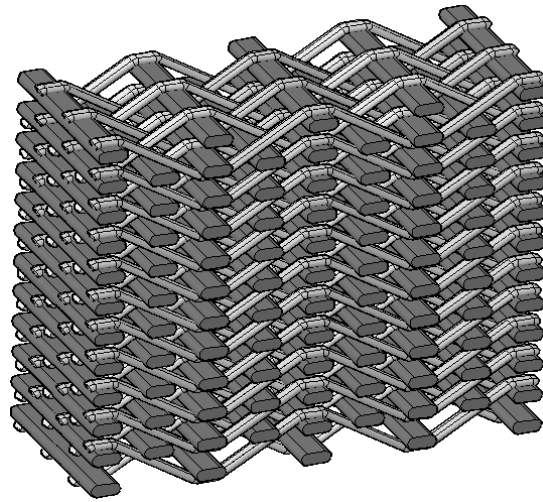
(a) 3-D angle-interlock structure

(b) axis line of warp yarn

Figure 4: 3-D angle-interlock structure and axis line of warp yarn of the 3-D angle-interlock woven composite

In order to find a balance between the microstructure model and the computer capacity, a continuum model has been established and merged with the microstructure model. Fig.6 shows the merged geometrical model. In Fig.6, one-quarter of the whole 3DAWC composite panel and the projectile were presented. In the composite panel, the 40×40mm panel was the microstructure model, while the rest parts of the composite panel are the continuum model. The continuum model has the same mechanical properties with the 3DAWC in experimental.
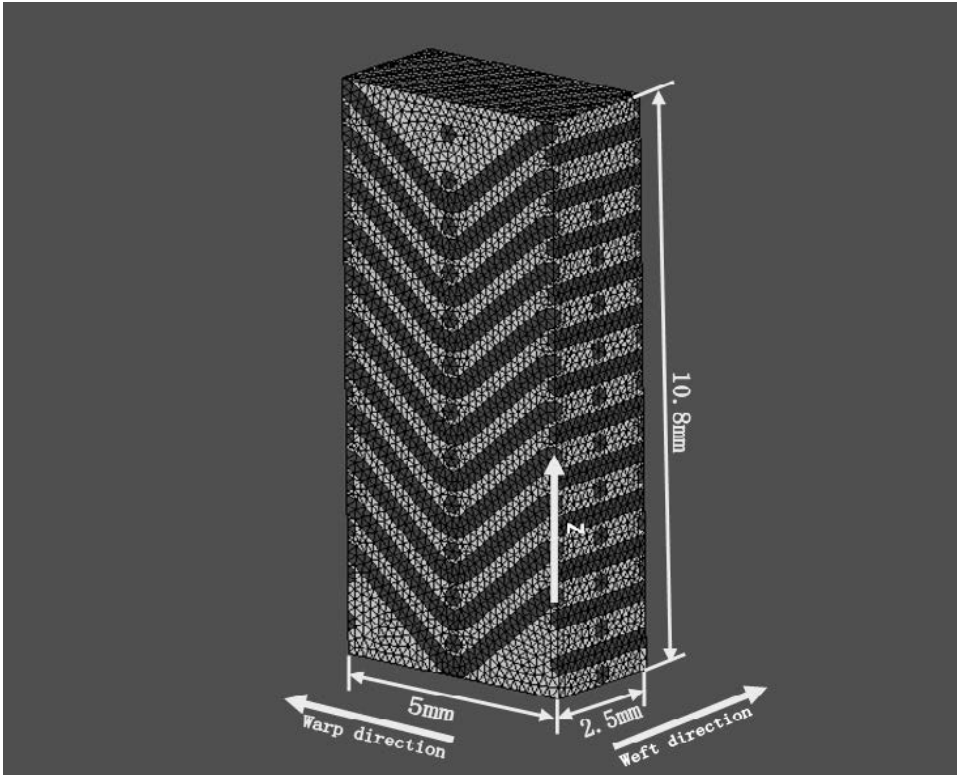
Figure 5: Mesh scheme of the 3DAWC microstructure model

As shown in Fig.7, the microstructure model and the continuum model shares the same node in finite element model during meshing.

3.3   Mesh scheme

In the multi-scale geometrical model, the microstructure model of the 3DAWC was meshed with the four-node tetrahedron elements. There are 10044800 elements and 2277571 nodes in this area. The continuum model was meshed with hexahedron elements. There are 1575840 elements and 1622247 nodes. The projectile was also meshed with hexahedron elements. There are 521760 elements and 527098 nodes in the projectile.

4   Algorithms

The interaction between a rigid projectile and 3DAWC target involves the sliding, erosion and deformation at the interface. Interfaces can be defined in three di-
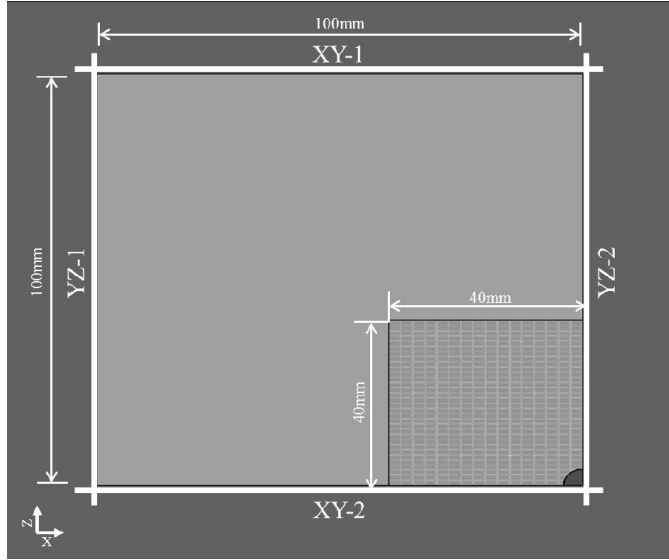
Figure 6: Combination of the microstructure model and the continuum model

mensions by listing in arbitrary order all triangle and quadrilateral segments that comprise each side of the interface. One side of the interface is designated as the slave side, and the other is designated as the master side. Nodes lying in those surfaces are referred to as slave and master nodes respectively [Hallquist (1998)].

The impact dynamics and concerned finite element algorithms have been reported in many books intensively in very large length, such as [Hallquist (1998), Belytschko, Liu and Moran (2000) and Zukus (1982)]. The algorithms can be simplified and described concisely as follows.

Fig.8 shows the impact of two bodies and the sliding surface between them. In a fixed rectangular Cartesian coordinate system, the position of an arbitrary point at time $t = 0$ is $X_i(i = 1, 2, 3)$. At time t the new position is $x_i(i = 1, 2, 3)$. The equation for the movement of the point is:

$$x_i = x_i(X_j, t) \text{ i, j} = 1,2,3 \tag{3}$$

At time $t = 0$:

$$x_i(X_j, 0) = X_i \\ \dot{x}_i(X_j, 0) = V_i(X_j, 0) \tag{4}$$

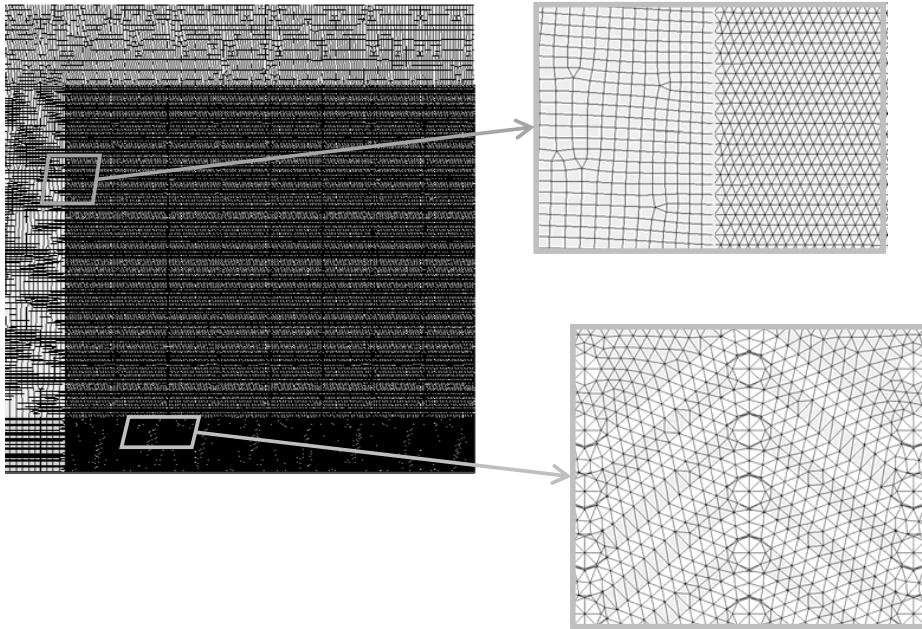where V_i is the initial velocity

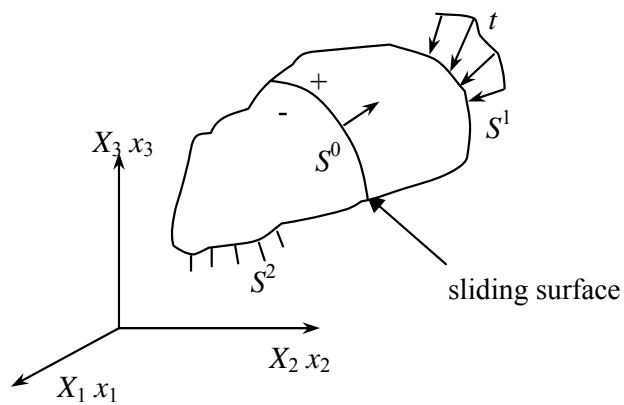Figure 7: Merge of the microstructure model and the continuum model
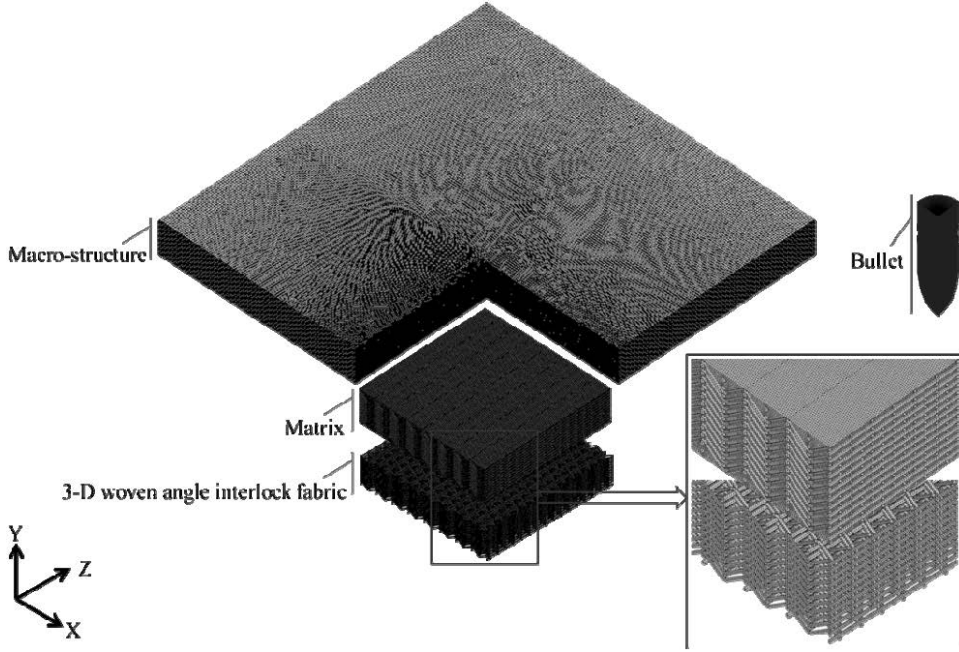

Figure 8: Contact notations

Figure 9: FEM model of quarter of the whole composite panel

4.1 Governing equations

We seek a solution to the momentum equation

$$\sigma_{ij,j} + \rho f_i = \rho \ddot{x}_i \tag{5}$$

satisfying the contact discontinuity

$$\left(\sigma_{ij}^+ - \sigma_{ij}^- \right) n_i = 0 \tag{6}$$

along an interior boundary $x_i^+ = x_i^-$. Here σ_{ij} is the Cauchy stress, ρ is the current density, f is the body force density, $\ddot{x}$ is the acceleration, the comma denotes covariant differentiation, and n_i is a unit outward normal to a boundary element.

Mass conservation is trivially stated

$$\rho V = \rho_0 \tag{7}$$

where V is the relative volume, i.e., the determinant of the deformation gradient matrix, F_{ij},

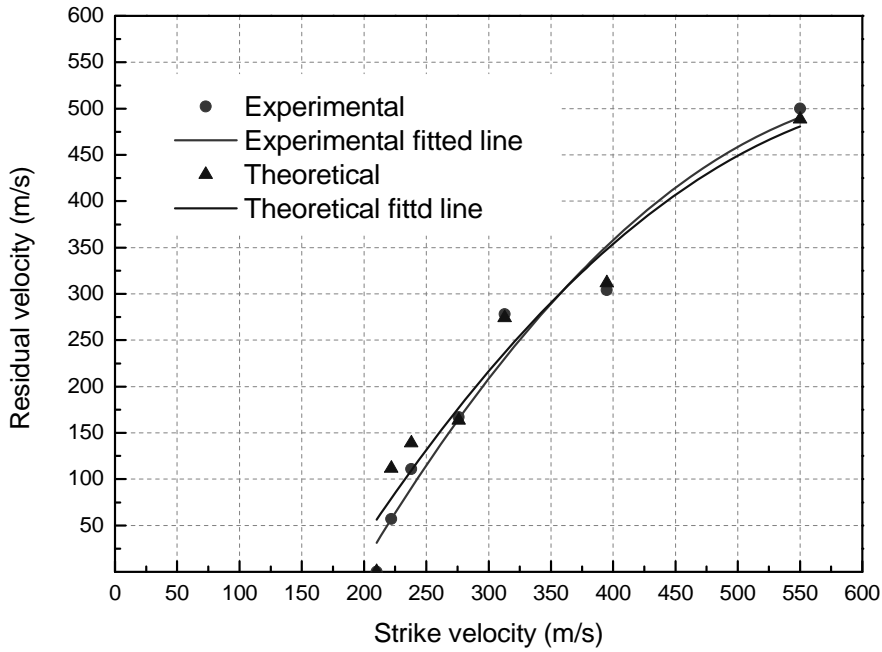$$F_{ij} = \frac{\partial x_i}{\partial X_j} \tag{8}$$

Figure 10: Strike velocity vs. residual velocity curves in FEM and experimental

and ρ_0 is the reference density. The energy equation

$$\dot{E} = VS_{ij}\dot{\varepsilon}_{ij} - (p+q)\dot{V} \tag{9}$$

is integrated in time and is used for equation of state evaluations and a global energy balance. In Equation (9), s_{ij} and p represent the deviatoric stresses and pressure respectively,

$$\begin{aligned} S_{ij} &= \sigma_{ij} + (p+q)\delta_{ij} \\ p &= -\tfrac{1}{3}\sigma_{ij}\delta_{ij} - q = -\tfrac{1}{3}\sigma_{kk} - q \end{aligned} \tag{10}$$

q is the bulk viscosity, δ_{ij} is the Kronecker delta and $\dot{\varepsilon}_{ij}$ is the strain rate tensor. The discussion on the advantage of bulk viscosity in numerical calculation of impact dynamics could be found in Ref. [Belytschko, Liu and Moran (2000)] and Ref. [Zukus (1982)].

We can write:

$$\int\limits_V (\rho\ddot{x}_i - \sigma_{ij,j} - \rho f_i)\delta x_i dV + \int\limits_{S^0} (\sigma_{ij}^+ - \sigma_{ij}^-)n_j \delta x_i dS + \int\limits_{S^1} (\sigma_{ij}n_j - t_i)\delta x_i dS = 0 \tag{11}$$

where δx_i satisfies all boundary conditions on S^2, and the integrations are over the current geometry. Applications of the divergence theorem gives

$$\int_V (\sigma_{ij}\delta x_i)_{,j}dV = \int_{S^1} \sigma_{ij}n_j\delta x_i dS + \int_{S^0} (\sigma_{ij}^+ - \sigma_{ij}^-)n_j\delta x_i dS \tag{12}$$

and noting that

$$(\sigma_{ij}\delta x_i)_{,j} - \sigma_{ij,j}\delta x_i = \sigma_{ij}\delta x_{i,j} \tag{13}$$

leads to the weak form of the equilibrium equations:

$$\delta\pi = \int_V \rho\ddot{x}_i\delta x_i dV + \int_V \sigma_{ij}\delta x_{i,j}dV - \int_V \rho f_i\delta x_i dV - \int_{S^1} t_i\delta x_i dS = 0 \tag{14}$$

a statement of the principles of virtual work.

4.2 Finite element discretization

We superimpose a mesh of finite element interconnected at nodal points on a reference configuration and track particles through time, i.e.,

$$x_i(X_j,t) = x_i(X_j(\xi,\eta,\zeta),t) = \sum_{j=1}^k \phi_j(\xi,\eta,\zeta)x_i^j(t) \tag{15}$$

where ϕ_j are the shape functions of the parametric coordinates (ξ,η,ζ), k is the number of nodal points defining the element, and x_i^j is the nodal coordinate of the jth node in the ith direction.

Summing over the n elements we may approximate $\delta\pi$ with

$$\delta\pi = \sum_{m=1}^n \delta\pi_m = 0 \tag{16}$$

and write

$$\sum_{m=1}^n \{\int_{V_m} \rho\ddot{x}_i\Phi_i^m dV + \int_{V_m} \sigma_{ij}^m\Phi_{i,j}^m dV - \int_{V_m} \rho f_i\Phi_i^m dV - \int_{S^1} t_i\Phi_i^m dS\} = 0 \tag{17}$$

where

$$\Phi_i^m = (\phi_1, \phi_2, \cdots, \phi_k)_i^m \tag{18}$$

In matrix notation Equation (17) becomes

$$\sum_{m=1}^{n} \{ \int_{V_m} \rho \mathbf{N}^t \mathbf{N} \mathbf{a} dV + \int_{V_m} \mathbf{B}^t \sigma dV - \int_{V_m} \rho \mathbf{N}^t \mathbf{b} dV - \int_{S^1} \mathbf{N}^t \mathbf{t} dS \}^m = 0 \tag{19}$$

where **N** is the interpolation matrix, σ is the stress vector

$$\sigma^t = (\sigma_{xx}, \sigma_{yy}, \sigma_{zz}, \sigma_{xy}, \sigma_{yz}, \sigma_{zx})$$

B is the strain-displacement matrix, **a** is the nodal acceleration vector

$$\begin{bmatrix} \ddot{x}_1 \\ \ddot{x}_2 \\ \ddot{x}_3 \end{bmatrix} = \mathbf{N} \begin{bmatrix} a_{x_1} \\ a_{y_1} \\ \vdots \\ a_{y_k} \\ a_{z_k} \end{bmatrix} = \mathbf{N} \mathbf{a} \tag{20}$$

b is the body force load vector, and **t** are applied traction loads

$$\mathbf{b} = \begin{bmatrix} f_x \\ f_y \\ f_z \end{bmatrix}, \quad \mathbf{t} = \begin{bmatrix} t_x \\ t_y \\ t_z \end{bmatrix}$$

After the finish of element calculation and assembly, Equation (17) could be written as:

$$\mathbf{M}\ddot{\mathbf{x}}(t) = \mathbf{P}(\mathbf{x}, t) - \mathbf{F}(\mathbf{x}, \dot{\mathbf{x}}) \tag{21}$$

where **M** is the global mass matrix, $\ddot{\mathbf{x}}(t)$ is the global nodal acceleration vector, **P** is the global load vector, and

$$\mathbf{F} = \sum_{m=1}^{n} \int_{V_m} \mathbf{B}^t \sigma dV$$

4.3   Calculating time

The calculation time required to finish the simulation depends on the mesh density. For a 8-node solid element, the critical time step size, Δt_e [Hallquist (1998)] is:

$$\Delta t_e = \frac{L_e}{Q + (Q^2 + C^2)^{1/2}} \tag{22}$$

where Q is a function of bulk viscosity coefficients C_0 and C_1:

$$Q = \begin{cases} C_1 c + C_0 L_e \left| \dot{\varepsilon}_{kk} \right| & \text{for } \dot{\varepsilon}_{kk} < 0 \\ 0 & \text{for } \dot{\varepsilon}_{kk} \geq 0 \end{cases} \tag{23}$$

L_e is characteristic length, and $L_e = v_e / A_{e \max}$

v_e, is the element volume, $A_{e \max}$ is the area of the largest side, and c is the adiabatic sound speed of element material (where $c = \left[\frac{4G}{3\rho} + \frac{\partial p}{\partial \rho} \right]^{\frac{1}{2}}$), ρ is the specific mass density.

For the 8-node solid element:

$$L_e = \frac{v_e}{A_{e \max}}$$

For the 4-node tetrahedron element:

$$L_e = \text{minimum altitude}$$

Both 8-node solid hexahedron element and 4-node tetrahedron element were used in finite element calculation. The minimum altitude of 4 node tetrahedron element is far less than that of 8 node hexahedron element because the mesh size of microstructure is far less than that of continuum model. Therefore the calculation time is determined by the minimum altitude of 4 node tetrahedron element.

For a material with m elements, the time step Δt at next calculating step is:

$$\Delta t^{n+1} = \alpha \cdot \min(\Delta t_{e1}, \Delta t_{e2}, \cdots \Delta t_{em}) \tag{24}$$

and the scale factor α at above Eq.(24) is 0.9 or small value for stability.

From Eq. (24), it is shown that the time required to finish calculation will become longer when element density is higher, while the calculating results will be closer to the actual situation. The element sizes were different according to different regions, and the contact area between the bullet and the composite was meshed in finer sizes.

4.4 Finite element calculations

The environments of all the FEM simulations are as follows:

(1) Hardware: Workstation: Intel (R) Xeon (R) CPU X5482 3.2GHz 16G RAM;

(2) Software.

The operation system platform is Windows Microsoft Windows XP Professional x64 Edition. All the geometrical models were created with Pro/E® Wildfire 5.0 and meshed with Altair® Hyperworks® version 10.0 Hypermesh. The FEM solver is LS-DYNA version 971 and the FEM postprocessor: is LS-PrePost 3.0-X64.

5   Results and discussions

5.1   *Residual velocities of projectile after ballistic penetration*

Fig.9 is the whole FEM model for the impact penetration calculations. For a given striking velocity of the projectile, the residual velocity can be calculated and compared with that in experimental. Fig.10 is the comparison of the strike velocity vs. the residual velocity curves between FEM and experimental. The residual velocities from FEA agree well with those in experimental although the differences exist at low and high strike velocity ranges. This means that the FEA model agrees well with that in ballistic tests and could be used in the 3DAWC ballistic limit estimation. The difference between the FEA and experimental mainly exists at the low strike velocity range and the high strike velocity range, especially when the strike velocity is lower than 250m/s. The reason for this difference most probably attributes to the Twaron® fiber tows were regarded as a continuum rod in FEM while they are composed of thousands of filament in each tow. The un-simultaneous failure of each filament and interface debonding will lead the higher energy absorption in experimental.

Fig.11 shows the velocity vs. time history and the acceleration vs. time history of the projectile during penetration. The penetration time is longer when the strike velocity is lower. Therefore, the projectile takes longer time to perforate the composite target at lower strike velocity. The absolute value of acceleration is greater when the strike velocity is higher. The fluctuation of the acceleration means the forces acted on the projectile is fluctuated. The non-simultaneous failures of the fiber tows during penetration lead to the fluctuation of the penetration resistance. This attributes to that the higher strike velocity, the lower penetration time. Then the stress waves at the cross-section points between the fiber tows are more difficult to reach the equilibrium state than that in longer penetration time. The non-equilibrium stress wave would induce the higher stress fluctuation for the breakages of fiber tows and resins in different time steps.

Furthermore, owing to the cylindrical-conically shape of the projectile, the penetration resistance of the 3DAWC acted on the projectile varies the shape of the projectile. When the conical part of the projectile finished penetrating the fabric, the acceleration reaches to a maximum value. The time corresponding to the maximum value will be later when the strike velocity is lower. This phenomenon is obviously shown in Fig.11.

5.2   *Impact damage evolution*

Fig.12 displays the impact deformation and damage of the 3DAWC target at the different time steps. Fig.13 is the stress propagation under impact. Owing to the
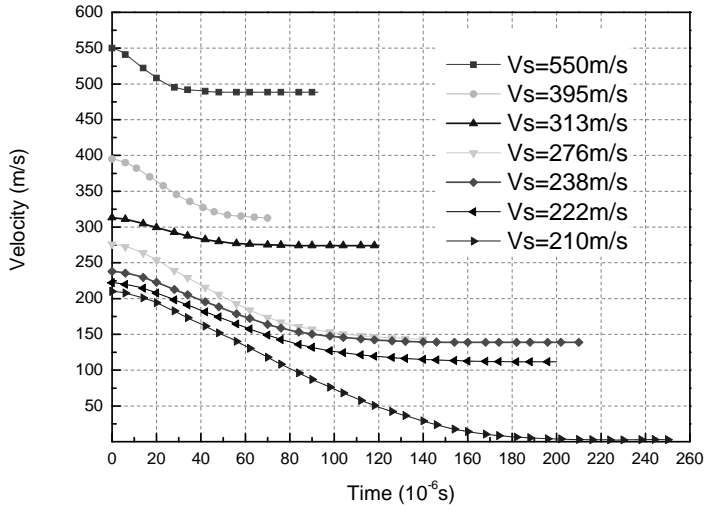
(a)
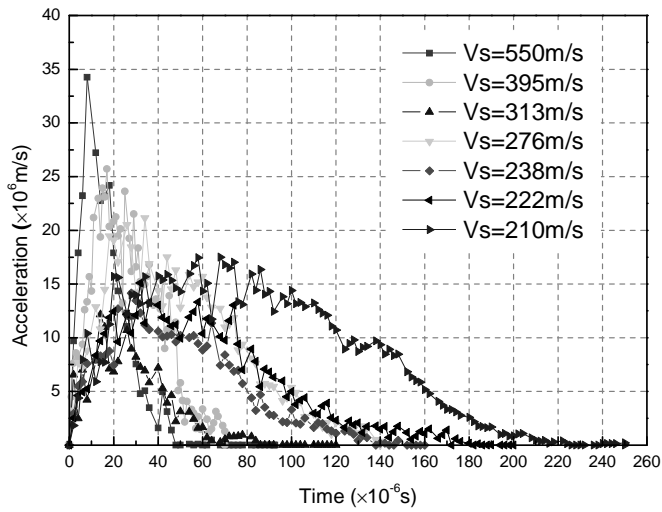
(b)

Figure 11: Velocity vs. time history and acceleration vs. time history of the projectile at the different strike velocities
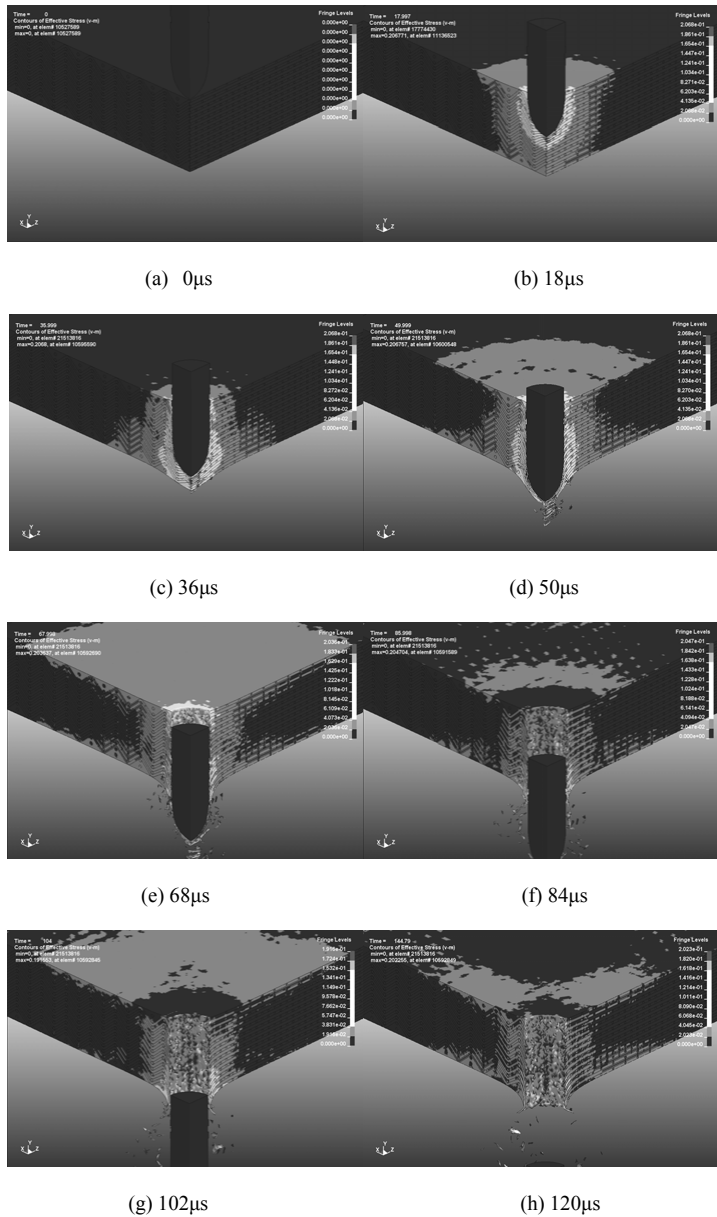
(a) 0μs   (b) 18μs

(c) 36μs   (d) 50μs

(e) 68μs   (f) 84μs

(g) 102μs   (h) 120μs

Figure 12: Ballistic penetration damage evolution of the composite panel under the impact velocity of 313m/s

(a) 0μs

(b) 20μs

(c) 30μs

(d) perforated
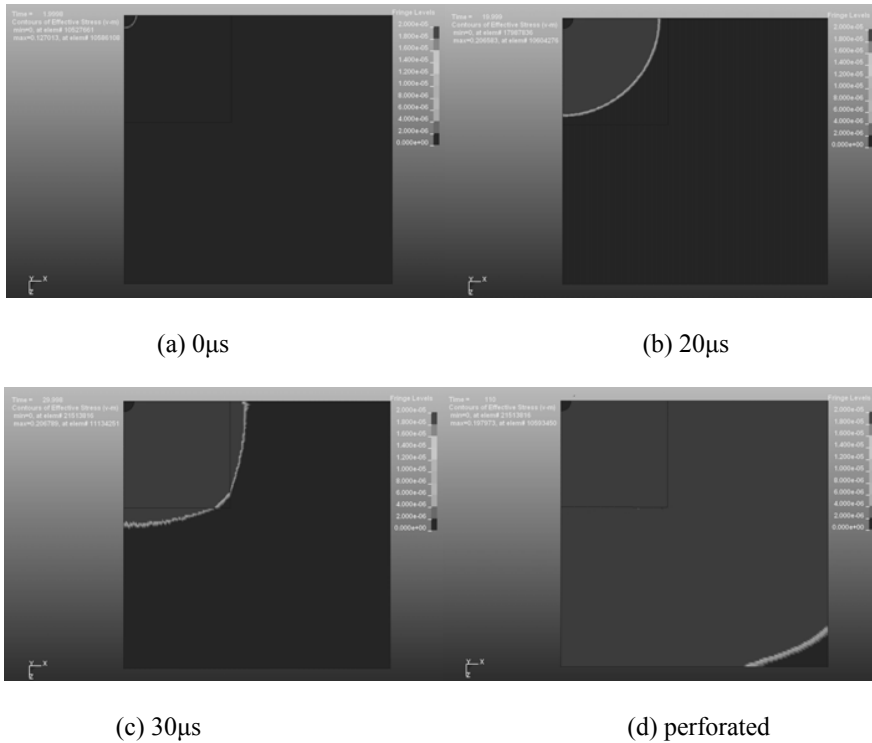
Figure 13: Stress wave propagation in the composite panel at different time steps

microstructure model and the continuum model share the same node at the interface, the stress wave will spread smoothly from the two phases. Fig.14 compares the impact damage between experimental and FEM.

In each time step, the impact damages are presented. The stress wave propagated along the fiber tows and resins and spread to the neighboring parts. In Fig.12, the extension of the fiber tows and the impact debris are clearly shown. From Fig.14, it is shown that there are much more damages occur on the top surface than on the rear surface, and the diameter of ballistic hole increases along the ballistic perforation direction. It can also be found that the FEA results agree well with the experimental results. There is no delamination in the 3DAWC which contrary to that of laminated composites. This distinct feature of the 3DAWC can be clearly shown in Fig.12 and Fig.14 (a).

5.3   Impact deformation

Fig.14 compares the final stage of the 3DAWC damage with the original fabric stage. In order to find the impact deformation of the 3DAWC panel, we chose the node No.2513287 as shown in Fig.15 for analyzing the deflection vs. time history. The deflection curves of this node under the different striking velocities were shown in Fig.16. The slope of the curves varied with the strike velocities. Under higher strike velocities, the time for reaching the maximum deflection will be shorter. At the striking velocity of 276m/s, the composite panel will be perforated in a little bit longer than that of 550m/s. Then the deflection is the greatest one. And for the striking velocities of 238, 222 and 210m/s, the deflection will be reached to stable value because the projectile will be arrested by the 3DAWC panel.

5.4   Stress propagation

Fig.17 shows the acceleration history of three nodes shown in Fig.15. The direction of the acceleration is along the normal direction which perpendicular to the 3DAWC panel plane. This acceleration history is also the stress history.

The acceleration vs. time history of the node 2513287 can be divided into 4 stages which shown in Fig.17 (a). For the four stages, there are four penetration depths as show in Fig.18. When the conical part of projectile begins to penetrate composite panel as shown in Fig.18 (a), the initial contact and penetration of the projectile will induce the stress in the 3DAWC. The fluctuation of the acceleration is from the element deletion in FEM calculation and from the fiber breakage, resin crack, interface debonding and the penal deformation in experimental. As the increase of the penetration depth, the fluctuation becomes greatly, as shown in the second stage, especially the whole conically part of the projectile penetrates into the composite panel, shown in Fig.18 (b). The third stage of the penetration consists of the penetrations both from the conically part and the cylindrical part of the projectile. This stage will induce the largest damage of the composite panel and also the greatest fluctuation of the acceleration curve. At the final stage shown in Fig.18 (d), the conically part of the projectile exits from the 3DAWC panel. Only the cylindrical part of the projectile stays in the 3DAWC panel. At this stage, the composite panel has been perforated. The only penetration resistance to the projectile is the friction between the composite and the projectile. The fluctuation of the acceleration becomes less than that in the third stage.
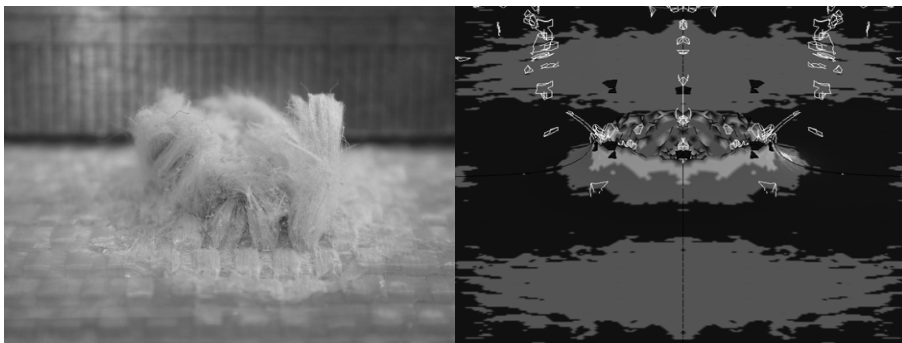
Compared Fig.17 (a) with Fig.17 (b), there is a time lag for the accelerations of the nodes No.3543183 and No.3848553. This is owing to the distance of the two nodes to the impact point is greater than that of the node No.2513287 as shown in Fig.15. The time lag is that the time difference of the stress wave propagates from
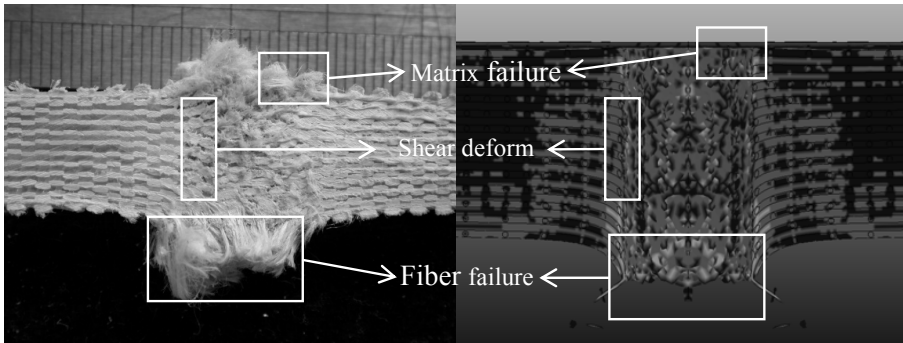
(a) Cross section view
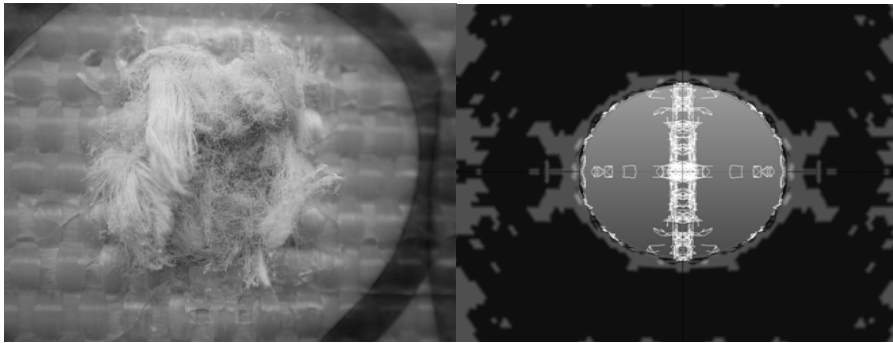
(b) Front surface view

(c) Rear surface 45° view

Figure 14: Comparisons of impact damage morphology under the strike velocity of 313m/s between experimental and theoretical
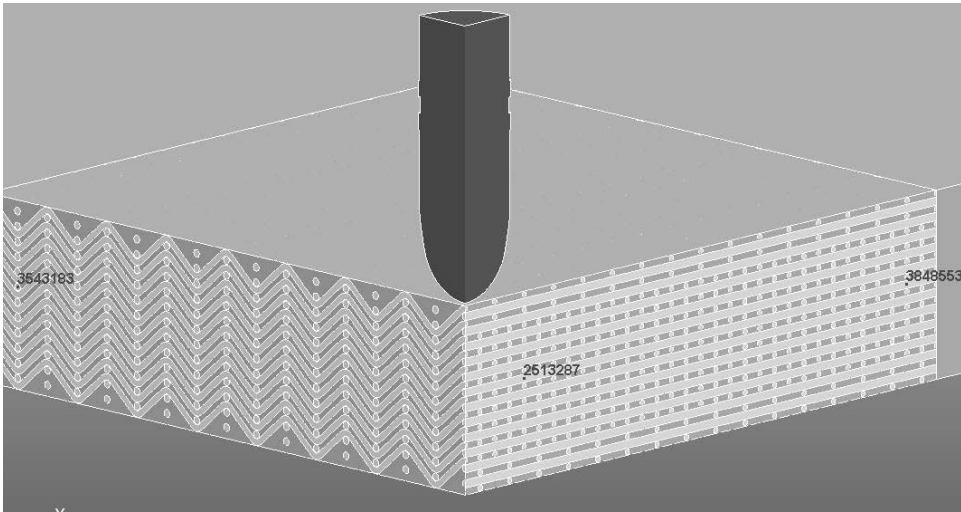
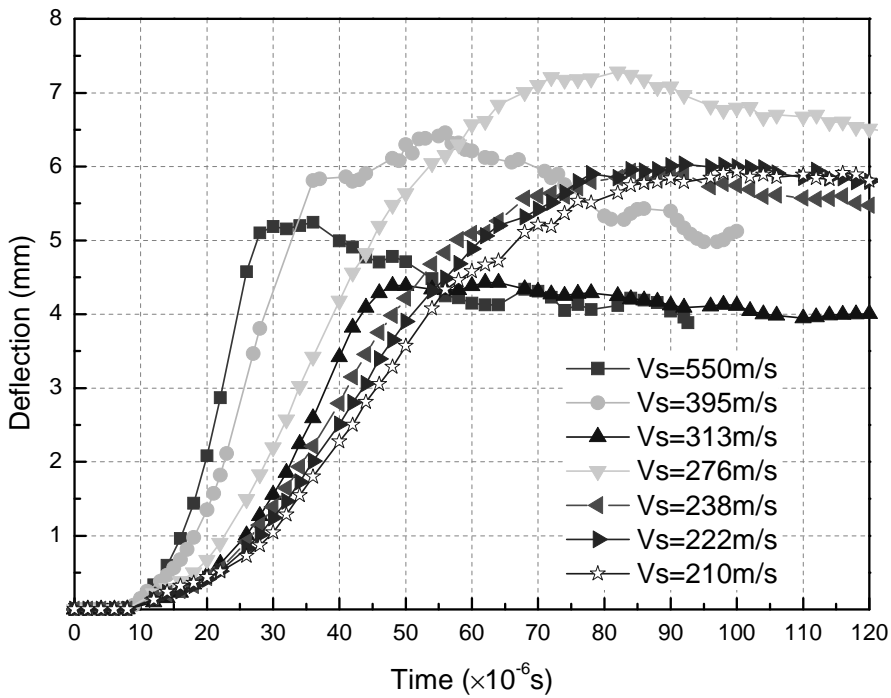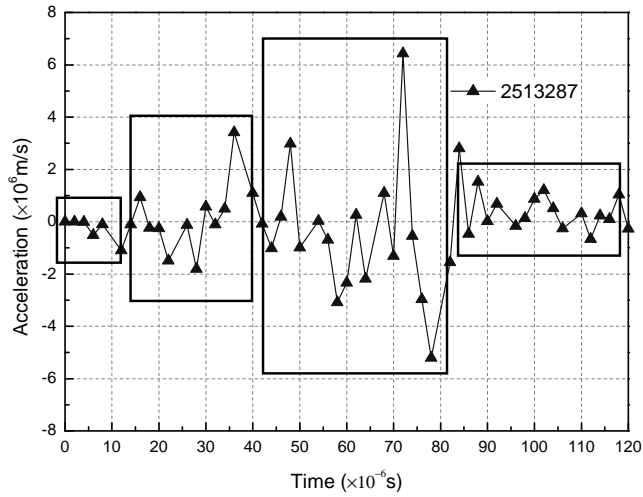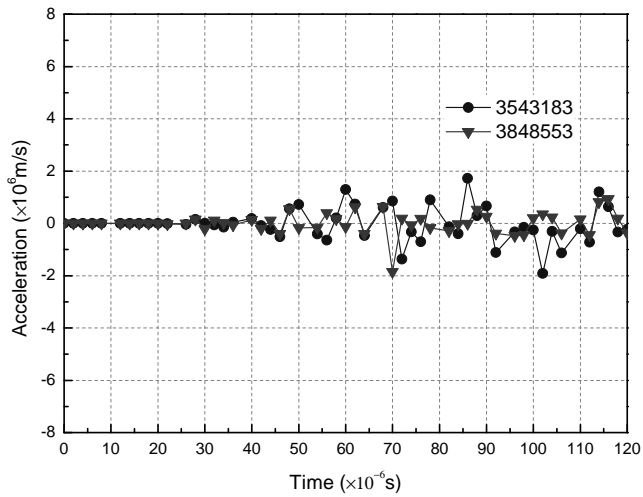Figure 15: Locations of the three selected nodes

Figure 16: Deflection of the node No.2513287 at the different strike velocities

(a)

(b)

Figure 17: Acceleration vs. time history curve of the selected nodes at the striking velocity of 313m/s (a) acceleration history of the node No.2513287; (b) acceleration history of the nodes No.3543183 and No. 3848553
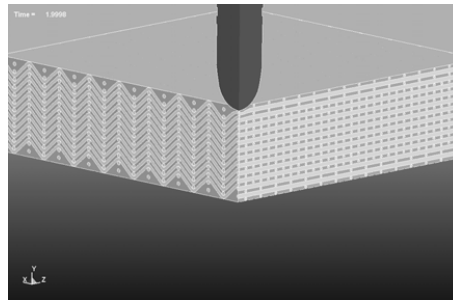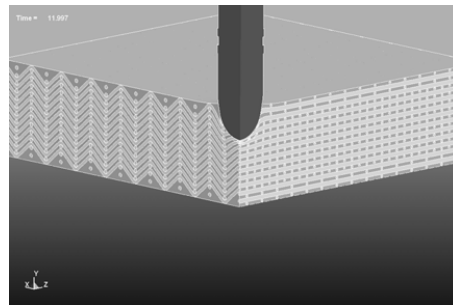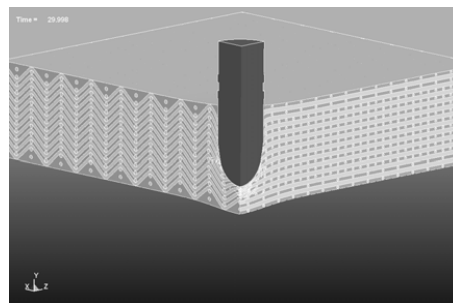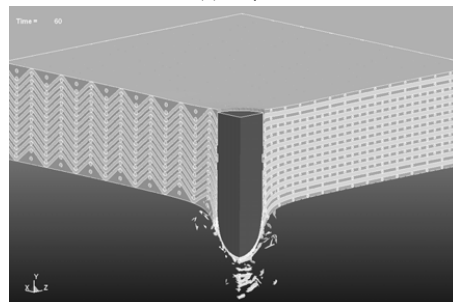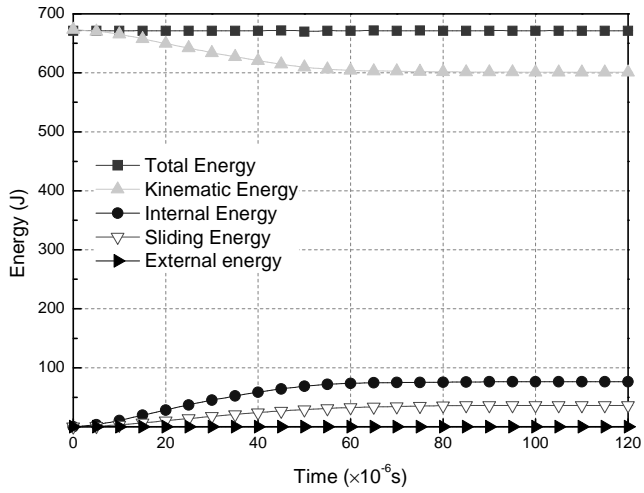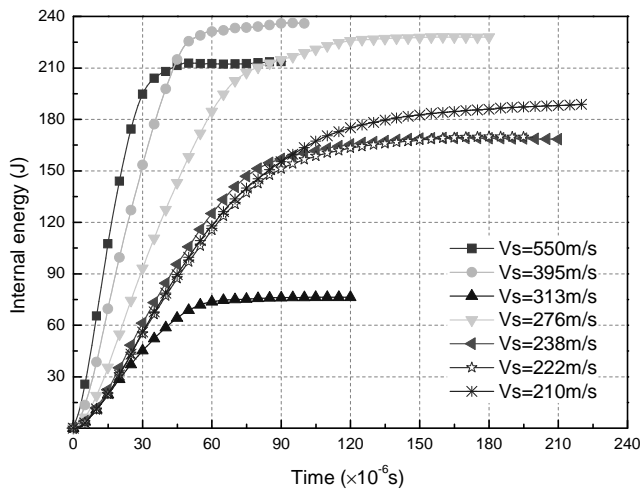
(a) 2 µs

(b) 12 µs

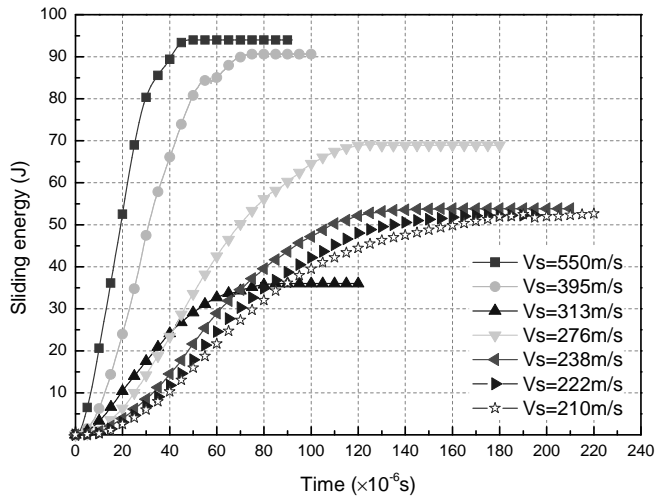(c) 30 µs

(d) 60 µs

Figure 18: Ballistic penetration at four different time steps

(a)

(b)

(c)

Figure 19: Energy vs. time history of the FEM model (a) decomposition of the total energy of the projectile-target system under the strike velocity of 313m/s; (b) internal energy vs. time curve under the different strike velocities; (c) sliding energy vs. time history under the different velocities

impact point to the node No.2513287 and to the nodes No.3543183, No.3848553. Furthermore, as the decay of the stress wave, the magnitude of the acceleration also decays.

5.5 *Energy absorption*

Fig.19 is the decomposition of the total energy of the 3DAWC under ballistic impact and shows that the main type of energy absorption in the 3DAWC is sliding energy and internal energy except the kinematic energy. As shown in Fig.19 (b) and (c), the sliding energy and internal energy increase with the impact velocity. This means the damages of the 3DAWC become much more severe with the increase of impact velocity. As discussed by Rao [Rao, Nilakantan, Keefe, Powers and Bogetti (2009)], the global-local deformation for the multi-scale geometrical model will induce the different tendencies of the sliding energy and internal energy at the different striking velocities. However, as shown in Fig.19 (c), the sliding energy increases with the striking velocity before the time of 60μs. At this time, the conically part of the projectile exited from the composite panel. The sliding energy

mainly depended on the friction and the striking velocity.

6   Conclusions

The present study successfully developed a preliminary, simple approach towards multi-scale global/local modeling to study ballistic impact onto a three-dimensional angle-interlock woven composite. In this model, the composite was computationally represented using a microstructure model around the impact point and a continuum model around the microstructure model. Under this modeling framework, the fiber volume fraction of the composite was maintained with that in experimental. With the modeling scheme, the ballistic penetration damages of the woven composite were calculated with FEM and compared with those in the experimental. In FEA calculation, the strike velocity vs. residual velocity curves of the steel conically-cylindrical projectile, energy absorption history curves, deformation and impact damage of the woven composite were obtained. In experimental, the residual velocities of the projectiles after ballistic perforation, damage morphologies of the composite plates, were measured and observed. Comparison between FEA and experimental results indicates that the microstructure model can predict the ballistic impact damage and energy absorption of the composite plate precisely. The failure modes are tensile and shear failure on the rear surface and compressive and shear failure on the top surface. The failure also includes the resin crack, fiber breakage and fiber pull-out. There is no delamination in the woven composite under ballistic impact because of the integrated structure of the three-dimensional angle-interlock woven fabric.

References

Barauskas, R.; Abraitiene, A. (2007): Computational analysis of impact of a bullet against the multilayer fabrics in LS-DYNA. *International Journal of Impact*

Engineering, vol. 34, no.7, pp. 1286-1305.

Belytschko, T.; Liu, W. K.; Moran, B. (2000): Nonlinear Finite Elements for Continua and Structures. New York: John Wiley & Sons, [Chapter 10].

Boussu, F. (2011): The use of warp interlock fabric inside textile composite protection against ballistic impact. *Textile Research Journal*, vol. 81, no. 4, pp. 344-354.

Chen, X. G.; Yang, D. (2010a): Use of 3D angle-interlock woven fabric for seamless female body armor: Part I: ballistic evaluation. *Textile Research Journal*, vol. 80, no. 15, pp. 1581-1588.

Chen, X. G.; Yang, D. (2010b): Use of Three-dimensional angle-interlock woven fabric for seamless female body armor: Part II: mathematical modeling. *Textile Research Journal*, vol. 80, no. 15, pp. 1589-1601.

Chiu, C. H.; Lai, M. H.; Wu, C. M. (2004): Compression failure mechanisms of 3-D angle interlock woven composites subjected to low-energy impact. *Polymer Composites*, vol. 12, no. 4, pp. 309-320.

Cui, F.; Sun, B. Z.; Gu, B. H. (2011): Fiber inclination model for finite element analysis of three-dimensional angle interlock woven composite under ballistic penetration. *Journal of Composite Materials*, vol. 45, no. 14, pp. 1499-1509.

Cuong, H. M.; Boussu, F.; Kanit, T.; Crepin, D.; Imad, A. (2011): Effect of frictions on the ballistic performance of a 3D warp interlock fabric: numerical analysis. *Applied Composite Materials*, DOI: 10.1007/s10443-011-9202-2 (to be appeared).

Gama, B. A.; Bogdanovich, A. E.; Coffelt, R. A.; Haque, M. J.; Rahman, M.; Gillespie, J. W. (2005): Ballistic impact damage modeling and experimental validation on a 3-D orthogonal weave fabric composite. International SAMPE Symposium and Exhibition (Proceedings, SAMPE 05: New Horizons for Materials and Processing Technologies - Conference Proceedings), Long Beach, CA, United states, Vol. 50, pp. 1161-1175.

Hallquist, J. O. (1998): Ls-Dyna Theoretical Manual. *Livermore Software Technology Corporation.* pp. 18.1-18.7, pp. 19.1-19.2.

Jin, L. M.; Sun, B. Z.; Gu, B. H. (2011): Finite element simulation of three-dimensional angle-interlock woven fabric undergoing ballistic impact. *Journal of the Textile Institute*, vol.102, no.11, pp. 982-993.

Kim, S. J.; Ji, K. H.; Paik, S. H. (2008): Numerical simulation of mechanical behavior of composite structures by supercomputing technology. *Advanced Composite Materials*, vol. 17, no. 4, pp. 373-407.

Ko, F. K.; David, H. (1986): Impact behavior of 2-D and 3-D glass/epoxy composites. *SAMPE Journal*, vol. 22, no.4, pp. 26-30.

Kuo, W. S.; Lee, L. C. (1998): Impact response of 3-D woven composites reinforced by consolidated rods. *Polymer Composites*, vol. 19, no. 2, pp. 156-165.

Li, Z. J.; Sun B. Z.; Gu, B. H. (2010): FEM simulation of 3D angle interlock woven composite under ballistic impact from unit cell approach. *Computational Material Science*, vol. 49, no. 1, pp. 171-183.

Nilakantan, G.; Keefe, M.; Bogetti, T. A.; Gillespie, J. W. (2010): Multiscale modeling of the impact of textile fabrics based on hybrid element analysis. *International Journal of Impact Engineering*, vol. 37, no. 10, pp. 1056-1071.

Nilakantan, G.; Keefe, M.; Bogetti, T. A.; Adkinson, R.; Gillespie, J. W. (2010): On the finite element analysis of woven fabric impact using multiscale modeling techniques. *International Journal of Solids and Structures*, vol. 47, no. 17, pp. 2300-2315.

Nadler, B.; Papadopoulos, P.; Steigmann, D. J. (2006): Multiscale constitutive modeling and numerical simulation of fabric material. *International Journal of Solids and Structures*, vol. 43, no. 2, pp. 206-221.

Rao, M. P.; Nilakantan, G.; Keefe, M.; Powers B. M.; Bogetti, T. A. (2009): Global/local modeling of ballistic impact onto woven fabrics. *Journal of Composite Materials*, vol. 43, no. 5, pp. 445-467.

Sun, B. Z.; Gu, B. H. (2007): Frequency analysis of stress waves in testing 3-D angle-interlock woven composite at high strain rates. *Journal of Composite Materials*, vol. 41, no. 24, pp. 2915-2938.

Tabiei A.; Ivanov I. (2007): Micro-mechanical model with strain-rate dependency and damage for impact simulation of woven fabric composites. *Mechanics of Advanced Materials and Structures*, vol. 14, no. 5, pp. 365-377.

Tserpes, K. I.; Labeas, G.; Pantelakis, S. (2010): Multi-scale modeling of the mechanical response of plain weave composites and cellular solids. *Theoretical and Applied Fracture Mechanics*, vol. 54, no. 3, pp. 172-179.

Zhang, Y. X.; Zhang, H. S. (2010): Multiscale finite element modeling of failure process of composite laminates. *Composite Structures*, vol. 92, no. 9, pp. 2159-2165.

Zohdi, T. I.; Powell, D. (2006): Multiscale construction and large-scale simulation of structural fabric undergoing ballistic impact. Computer *Methods in Applied Mechanics and Engineering*, vol. 195, no. 1-3, pp. 94-109.

Zukus, J. A. (1982): Penetration and perforation of solids. Impact dynamics. New York: John Wiley, pp. 155-214, 377-382.